# Atomically Resolved Edges and Defects in Lead Halide Perovskites

Biao Yuan[1,5,6†], Zeyu Wang[2†], Shuchen zhang[3,4†], Christoph Hofer[1], Chuang Gao[1], Tamazouzt Chennit[1], Hongshen Shi[2], Xiaoyan Wu[2], Yu Han[5,6], Letian Dou[4*], Yi Yu[2*], Timothy J. Pennycook[1*]

[1]Electron Microscopy for Materials Science, University of Antwerp, Groenenborgerlaan 171, Antwerp, 2020, Belgium.
[2]Shanghai Key Laboratory of High-resolution Electron Microscopy, ShanghaiTech University, 393 Middle Huaxia Road, Shanghai, 201210, China.
[3]Department of Materials Science and Engineering, University of Science and Technology of China, 96 JinZhai Road, Hefei, 230026, China.
[4]Davidson School of Chemical Engineering, Purdue University, 610 Purdue Mall, West Lafayette, 47907, Indiana, United States.
[5]Center for Electron Microscopy, South China University of Technology, 381 Wushan Road, Guangzhou, 510640, China.
[6]School of Emergent Soft Matter, South China University of Technology, 381 Wushan Road, Guangzhou, 510640, China.

*Corresponding author(s). E-mail(s): dou10@purdue.edu; yuyi1@shanghaitech.edu.cn; Timothy.Pennycook@uantwerpen.be;
†These authors contributed equally to this work.

**Abstract**

While edges and defects constitute only a small fraction of crystalline materials, they exert an outsized impact on materials properties. Organic-inorganic halide perovskites are promising next generation semiconductor materials with superior cost effectiveness and intriguing optoelectronic properties, however their edges have not previously been directly observed at atomic resolution due to their extreme sensitivity. Our approach, combining ptychography with dose fractionated ultra-lowdose acquisition reveals the edges at atomic-resolution at electron doses as low as tens of $e^{-}/Å^{2}$. A majority methylammonium (MA) and iodine (I) edge termination is observed in $MAPbI_3$. More importantly our imaging reveals different structural dynamics resulting from different edge and internal defects. We find that defects exert a considerable influence on the rate of damage, with a preponderance of I vacancies correlating with higher rates of damage.

**Keywords:** 4D-STEM, ptychography, electron beam sensitive, hybrid perovskite

# 1 Introduction

Organic-inorganic halide perovskites[1] have received particular attention for their potential in solar energy applications due to their high efficiency, ease of fabrication, tunable properties, and versatility.[2,3,4] However, addressing substantial challenges related to edges, defects and stability is critical to achieving their potential.[5,6,7,8] Halide perovskites take the form $ABX_3$, where A represents a monovalent cation, B is a metal cation, and X denotes a halide anion. Each element plays a crucial but different role in perovskite stability,[9,10,11] however computational and experimental studies have identified undercoordinated B-sites as potentially the most destabilizing, and their passivation with diverse Lewis base molecules has been demonstrated to provide noteworthy enhancements in both stability and photovoltaic efficiency.[12,8,13] However, atomic-scale insights remain limited due to challenges in atomic-resolution imaging of these highly beam sensitive materials.[14] Furthermore, computational studies show the atomic distribution at the edges significantly influences both efficiency and stability,[15,16,13] , yet so far atomic-resolution imaging of their edges has remained elusive.

The primary challenge with imaging halide perovskites is beam damage. For example the organic-inorganic hybrid material $MAPbI_3$ (Methylammonium lead iodide) (Fig. 1b) begins to show damage in conventional plane-wave TEM at an extremely low dose (fluence) of 5.95 $e^-/Å^2$, less than one thousandth the dose typically used for stable samples.[14,17] However, similar structures show no apparent damage before 66 $e^-/Å^2$ using scanning transmission electron microscopy (STEM).[18] This suggests that the perovskites are more stable in STEM. Previous STEM studies utilised low-angle annular dark field (LAADF) imaging to maximize the Z-contrast signal in combination with a thick sample.[18] Defects consisting of only a few atoms are not visible in such a thick material, and we therefore used ultrathin $MAPbI_3$ instead. This is made possible with our new synthesis method.[19] Using ultrathin material allows us to detect the few-atom defects which initiate damage. As the LAADF signal is proportional to the thickness of a column, reducing thickness also reduces the signal and it is desirable to supplement the LAADF with the higher overall dose efficiency of electron ptychography.[20,21] Ptychography has greatly advanced in recent years, breaking resolution records.[22,23,24] However, so far the minimum dose used experimentally for atomic resolution ptychography was 403 $e^-/Å^2$,[25] far beyond the limits tolerable for $MAPbI_3$.

Here we present ultralow-dose imaging of ultrathin $MAPbI_3$, revealing for the first time the fine structural details of its edges and defects and their evolution during damage. We achieve this using 4D-STEM methods we developed to collect dose-fractionated 4D-STEM at the extreme scan speeds that minimize damage in halide perovskites. Our ptychography provides atomic resolution images at tens of $e^-/Å^2$ in which all types of atomic sites are visible. The dose-fractionation allows us to not only build signal up to the point that damage occurs, but most importantly, to observe the dynamics of the damage process and correlate structure with damage rates. Our results show that the (1 1 0) majority edge is terminated by MA-I and that $I^-$ vacancies are a primary driver of damage, initiating and accelerate structural collapse both at the edges and within the material.

# 2 Results

## 2.1 Ultralow-dose imaging of $MAPbI_3$

Fig. 1 illustrates our experimental setup. We use an event driven camera[26] to enable 4D-STEM with extremely rapid scans which in combination with a low probe current allow us to achieve very low doses. Given the extreme fragility of $MAPbI_3$, we compared wide-area parallel illumination TEM with very rapidly scanned STEM probes (SFigs. 6–9). Consistent with previous halide perovskite studies,[18] rapidly scanned

focused probes produce substantially less damage for a given dose. In fact using multiple scans the material withstands between five to ten times the dose than in TEM (see SI), suggesting its damage mechanism favours multiple very short exposures over continuous irradiation,[27] and therefore also a focused probe.

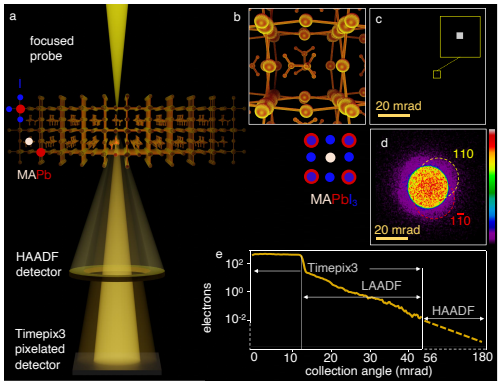


**Fig. 1 Ultralow-dose 4D-STEM imaging of $MAPbI_3$.** (a) Experimental setup. (b) The perovskite structure viewed along the electron beam direction, showing the $PbI_6^{4-}$ octahedra and $MA^+$ ions, which can tilt. (c) Individual CBED pattern consisting of a single hit, highlighted by the inset. (d) Position-summed CBED pattern from a 512×512 probe position scan. The colour bar ranges from 0 to 144, indicating the number of events per pixel after summing. (e) Logarithmic plot of the average number of electrons per unit angle as a function of collection angle, utilized in ptychographic phase imaging, low angle and high angle ADF imaging.

Keeping the probe moving as much as possible, each individual convergent beam electron diffraction (CBED) pattern contains only a single hit on average as illustrated in Fig. 1c, but when summed over the full dataset (Fig. 1d) one clearly sees the characteristic tetragonal pattern of $MAPbI_3$. Outside the central disk of the direct beam, the scattering rapidly diminishes with increasing angle. This illustrates how by integrating over lower angles LAADF is able to provide higher signal than high-angle ADF (HAADF). However, LAADF still must exclude the region with the most signal by far, the direct beam, and therefore does not make maximum use of the available information. In contrast ptychography makes use of the direct beam, and provides much greater overall dose efficiency.

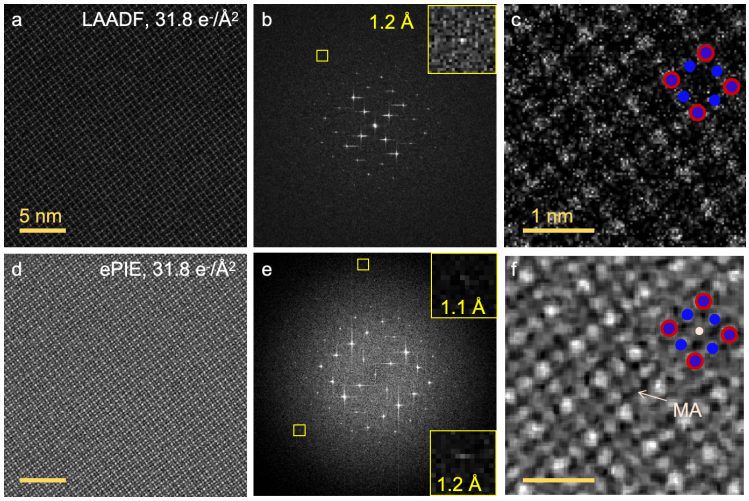


**Fig. 2 Atomic resolution imaging of $MAPbI_3$** with (a-c) LAADF, and (d-f) ePIE ptychography. dose: 31.8 $e^-/Å^2$. (b, e) Power spectra of a and e with boxes and insets showing the highest resolution spots. (c, f) Enlargements of the images in a and f.

Fig. 2 compares LAADF and ePIE[28] ptychography of our ultrathin $MAPbI_3$ produced from data utilizing 31.8 $e^-/Å^2$ dose fractionated over three scans. Subsequent scans show the transition from tetragonal to orthorhombic occurring (SFigs. 10, 21–23). Due to the Z-contrast, the strongly scattering heavy atomic columns are resolved in the LAADF images, but not the lighter MA columns. The ptychography however is more efficient, and its significantly clearer images allow us to reveal the locations of all the atomic columns, including the $MA^-$ molecules, as is also seen in simulations (SFigs. 24–27).

The ePIE algorithm was used because it converges even at the dose of the individual scans in our dose fractionated data (SFig. 28), when other iterative methods did not. It also provides slightly higher resolution than direct SSB ptychography (SFig. 29), likely from the inclusion of the higher angle scattering. However, converging iterative methods remains challenging and laborious under these conditions (see SI), and correct convergence is not guaranteed.[29] It is therefore useful to retain the fast reliable SSB and LAADF signals. Contrast reversals can occur in STEM phase imaging methods, resulting in dips on the heavy atomic columns.[30,31,32] These are expected for ultrathin $MAPbI_3$ and occur only on the PbI columns,[32] which remain clearly distinguished both in the ADF methods and the ptychography. However, to facilitate interpretability we apply our recently developed phase offset method[32] to remove these (see SI, SFig. 15-16).

## 2.2 Resolving edge structure in $MAPbI_3$

Fig. 3 shows the structure and evolution of an edge exposing the (1 1 0) plane, representing the majority of edges in $MAPbI_3$.[33] Data were collected continuously for 12 scans at approximately 11 $e^-/Å^2$ per scan, with the displayed reconstructions performed by combining every three scans to enhance the signal with an acceptable loss of time-resolution given the dynamics observed in the individual scans. The majority of the edge is terminated by the I-MA layer indicted by the blue arrow in Fig. 3a. This is consistent with our observations of I-MA termination other regions (e.g. SFig. 34-35), as well as with DFT calculations[34,35] showing this termination is energetically favourable.

In the initial scans, the I sites in the terminating layer are significantly darker in region 1 than region 2, indicative of a greater density of vacancies in region 1. This is apparent in Fig. 3a and the lateral unit cell averaging over the three unit cell wide regions 1 and 2 within it (Fig. 3b). Fig. 3c shows ptychography simulations based on the displayed three unit cell thick model at 100 $e^-/Å^2$, close to the effective 99 $e^-/Å^2$ obtained by averaging across three unit cells at 33 $e^-/Å^2$. In this model, fully occupied I sites in the I-MA layers have six I atoms, and 1–5 I vacancies have been introduced at the edge. The change in occupancy is apparent in the ptychographic simulations, confirming that the reduced brightness of the I sites in region 1 are due to I vacancies.

Additional scans can be seen to damage region 1 substantially more than region 2 as shown in Fig. 3d–e and SFigs. 36–38. Region 1 exhibits both loss of material and formation of Pb crystallite (red box, Fig. 3e). Region 2, however, retains the perovskite structure with significantly lower loss of edge atoms, suggesting that the different terminations have a strong impact on stability, with edge vacancies in Region 1 significantly increase the damage rate.

Observing additional edge regions we find that those with similarly few I vacancies as region 1 in Fig. 3 exhibit similar stability. SFig. 34 contains a region in which the MA occupation appears reduced at the edge, but has overall a similar I occupancy as the rest of the edge and damages at a similar rate. This suggests that I vacancies have a greater impact on the stability, which fits with the bonds between I and Pb being much stronger and more important to the crystal framework than the loosely bound MA molecules.

We find that other regions with a similar edge I vacancy concentration to region 1 damage at a similarly rapid rate, such as the defect on the left side of SFig. 41. The right side of the figure shows an edge region with what appears to be an even

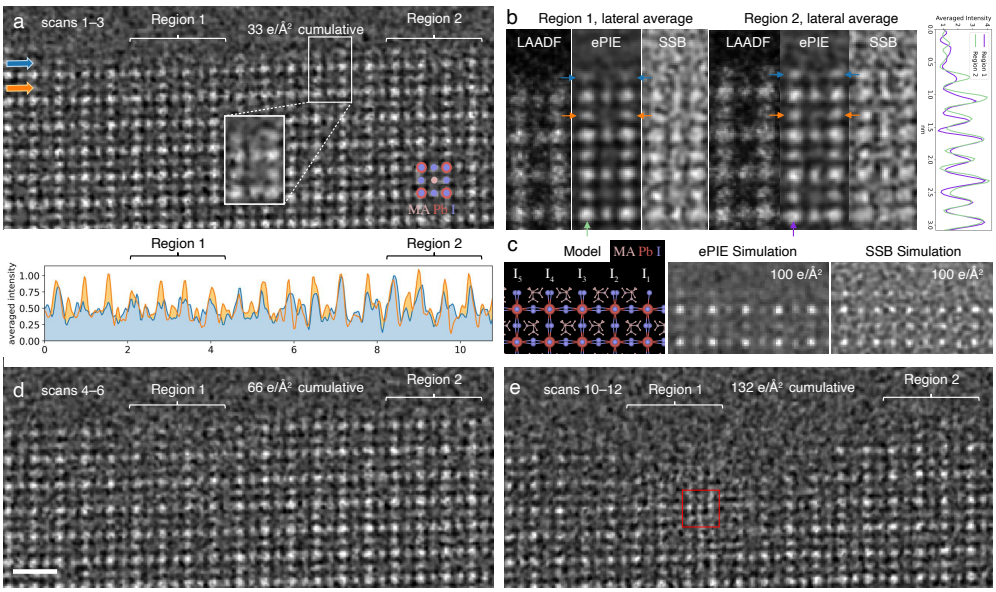


**Fig. 3 Edge structure and evolution in $MAPbI_3$** Dose fractionated data collected at 11 $e^-/Å^2$ per scan. (a) ePIE image from before the onset of signifiant damage showing significant variation in the occupancy of the terminating I-MA layer. The line profiles compare the terminating layer (blue) and the next I-MA layer back from the edge (orange). (b) Lateral unit cell average images of regions 1 and 2 in (a) more clearly showing the difference in occupation at the edge. (c) Ptychography simulations based on the displayed model with the indicated I site occupations. (d) and (f) ePIE images from scans 4-6 and 10–12, in which the cumulative effect of 66 and 132 $e^-/Å^2$ dose can be seen. Substantial damage starts in the more edge vacancy dense region 1 and expands, while region 2 is much more robust. The red box highlights a Pb crystallite formed by the damage. Scale bar 1 nm.

greater concentration of vacancies in the first scan. This region damages so quickly that it has already substantially degraded by 32.5 $e^-/Å^2$, and the damage very rapidly expands in subsequent scans. These observations underscore the significant impact of edge structure on stability, with areas containing greater concentrations of I vacancies damaging significantly more rapidly than those with lower concentrations.

## 2.3 Interior region defects

Defects within the interior of the crystal can also strongly affect stability. Rather than transitioning to orthorhombic after 32 $e^-/Å^2$, this region damages much more rapidly and severely, appearing to lose significant material in an area around five times the initial defect size by 128 $e^-/Å^2$. As the damage increases an area of Pb metal also emerges (SFig. 42). An even greater damage rate is observed for the two defects in SFig. 43. Both of these defects exhibit the spacings of $PbI_2$ in the first scans, consistent with a significant presence of I vacancies. They then both rapidly lose material and form Pb metal (see SI for details).

In contrast, the areas containing the defects in Figs. 4d and g remain stable to over 100 $e^-/Å^2$. They also do not appear to expand significantly as the dose increases further (SFig. 45). For instance the Fig. 4d defect expanded relatively little even after 209 $e^-/Å^2$. Areas of $PbI_2$ appear elsewhere in the regions containing both defects above 100 $e^-/Å^2$, but they do not appear connected with the defects and seem more likely to have formed due to the ejection of I in the pristine areas.

We analysed the occupation of the defects in detail by quantifying the phases of the atomic sites in the images, which allows us to estimate a net ionic charge based on the balance of cations and anions (see SI). The destabilising defect in Fig. 4a, contains a high proportion of $I^-$ vacancies producing an estimated net ionic charge of +2.5. The stable defects in Fig. 4d and g however have a greater proportion of Pb vacancies resulting in charges of −0.86, and −0.13.

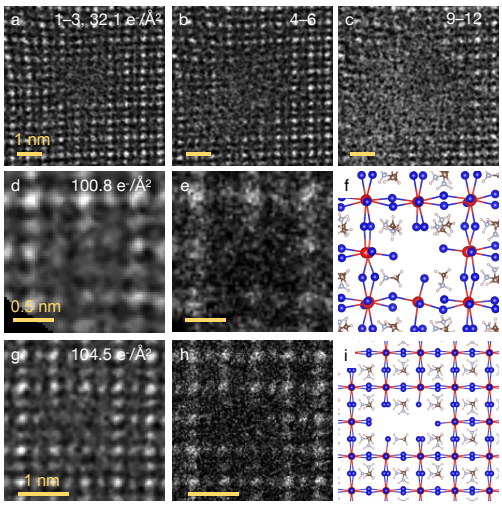


**Fig. 4** Defects in the internal regions of the material also significantly degrade stability. (a–c) ePIE phase images corresponding to the 1–3, 4–6, and 7–9 scans. The charge associated with the structure in a is estimated to be +2.5. (d, e) Enlarged ePIE image and LAADF image of a stable defect (charges: -0.86). (f) Corresponding potential crystal structure model. (g, h) Enlarged ePIE image and LAADF image of another stable defect (charges: -0.13). (i) Corresponding potential crystal structure.

# 3 Discussion

The most substantial damage to the crystal we observe occurs where significant I depletion occurs, and is often associated with the formation of $PbI_2$ or Pb metal. Chemically it makes sense that these form when sufficient I vacancies develop. Halide ion migration has been associated with damage in organic perovskites,[36,11] and this fits the observation that positively charged defects accelerated damage while negatively charged defects are more stable. $I^-$ halide ions will be attracted to a positive charge and repelled by a negative charge. These observations suggest the stability of $MAPbI_3$ could be enhanced with excess MAI during synthesis to reduce the formation of $I^-$ vacancies. Furthermore, they provide experimental evidence that that Lewis base molecules indeed improve stability by by passivating the uncoordinated $Pb^{2+}$ or positive charged centre with excess electrons.

In summary, we present the first atomically resolved imaging of the edges of an organic perovskite. Using dose-fractionated event driven 4D-STEM to perform the lowest dose atomic resolution ptychography to date, we reveal the details of the edge structure of ultrathin $MAPbI_3$ and its dynamics during damage. While simultaneous LAADF provides reliable atomic number contrast, ptychography provides a stronger signal for the lighter atomic columns that allows us to detect the small changes in occupancy that can trigger or accelerate damage. In particular, the damage rate increases with halide $I^-$ vacancy concentration, and is potentially slowed by the presence of $Pb^+$ vacancies. These findings provide much needed insight into the fragility of organic perovskites that were not previously possible to obtain. Furthermore, the methods we use will enable other fragile materials to be understood in unprecedented detail, especially materials that, like $MAPbI_3$, damage more rapidly under the continuous illumination of conventional TEM than multiple rapid STEM scans.

# 4 Methods

## 4.1 Synthesis of $MAPbI_3$ nanosheets

To synthesize the $MAPbI_3$ nanosheets for TEM characterization, an equilibrium solution conversion method reported in the article was used, and the 2D Ruddlesden-Popper phase perovskite, specifically $BA_2MA_2Pb_3I_{10}$, is utilized as a template. First, the solution to grow $BA_2MA_2Pb_3I_{10}$ single crystal was made using PbO (0.57 mmol), BAI (0.20 mmol) and MAI (0.44 mmol), which were dissolved in a mixture of 0.9 mL

HI and 0.1 mL $H_3PO_2$ in a 10 mL glass vial. This solution was kept at 45 °C and 2 –3 $\mu$L of this warm supernatant solution was collected with a 10 $\mu$L pipette and dispersed onto a glass slide placed in an open ambient environment (22 °C). Once the RP perovskite nanosheets formed on the surface of this solution, a copper TEM grid with ultra-thin carbon film (purchased from Beijing Zhongjingkeyi Technology Co., Ltd., BZ11033b) was used to gently pick them up and the thickness of RP perovskite nanosheets controlled by the precipitate time. Then, the corresponding TEM grid with 2D perovskite was dried for 10 min in a vacuum drier. After removing the excess solvents, the 2D perovskite sample was converted to $MAPbI_3$ nanosheets in a glass vial with a volume of 2 mL. By applying 300 $\mu$L equilibrium solution, made with $MAI/PbI_2$ in a 1:3 ratio, this conversion reaction proceeded for 17 min at room temperature. Once the conversion finished, the samples were annealed at 57 °C for 10 minutes. This conversion process was performed in a nitrogen-atmosphere glovebox.

## 4.2 TEM Characterization

Diffraction patterns were acquired on a 200 kV Tecnai Osiris with a Gatan US1000XP CCD camera. 4D-STEM data acquisition was conducted at 200 kV on an aberration-corrected Thermo Fisher Themis Z, equipped with an event-driven Timepix3 direct detection camera. The EELS measurements were performed on a 300 kV Thermo Fisher Titan. The dose-rate control was achieved by varying the mono focus, condenser aperture size and dwell time. The electron dose of 4D-STEM dataset was determined by the events on camera. The simulations were simulated with abTEM (https://abtem.readthedocs.io/en/stable/index.html), and 4D-STEM data were processed with pyPtychoSTEM (to generate SSB phase images, https://gitlab.com/pyptychostem/pyptychostem), and in house python code (to generate all the ePIE, WDD and iCoM results). The iteration step lengths for ePIE were carefully optimized for proper convergence, and scan positions were shuffled in each iteration to avoid periodic artifacts.

**Supplementary information.** Supplementary Text
Supplementary Table 1 to 2
Figs. S1 to S47

**Acknowledgements.** This work was supported by the funding from the European Research Council (ERC) under the European Union's Horizon 2020 Research and Innovation Program via Grant Agreement No. 802123-HDEM (T.J.P.) and Research Foundation Flanders (FWO) Project G013122N "Advancing 4D-STEM for atomic scale structure property correlation in 2D materials". Z.W and Y.Y acknowledge the funding from the National Natural Science Foundation of China (52222311), and the support from the centre for high-resolution Electron Microscopy at ShanghaiTech University. S.Z. and L.D. acknowledge the support from the US Department of Energy, office of Basic Energy Sciences under award number DE-SC0022082 (Materials Chemistry program). Y.H. acknowledges the financial support from the GJYC program of Guangzhou City for this research.

**Author contributions.** B.Y. and T.J.P. conceived the project and designed the experiments which B.Y. carried out and analysed; B.Y., Z.W., X.W. and Y.Y. performed iterative ptychography; S.Z. and L.D. synthesized the perovskite; C.H. and C.G. aided the 4D-STEM data acquisition and processing; T.C. and H.S. aided the simulations. B.Y. and T.J.P. wrote the manuscript. All authors read and reviewed the paper.

**Competing interests.** The authors declare no competing interests.

# References


[1] Dong, Y. *et al.* The role of surface termination in halide perovskites for efficient photocatalytic synthesis. *Angewandte Chemie* **132**, 13031–13037 (2020).

[2] Ahmadi, M., Wu, T. & Hu, B. A review on organic–inorganic halide perovskite photodetectors: device engineering and fundamental physics. *Advanced Materials* **29**, 1605242 (2017).

[3] Chen, J. *et al.* Highly efficient and stable perovskite solar cells enabled by low-dimensional perovskitoids. *Science Advances* **8**, eabk2722 (2022).

[4] Shi, E. *et al.* Two-dimensional halide perovskite nanomaterials and heterostructures. *Chemical Society Reviews* **47**, 6046–6072 (2018).

[5] Mariotti, S. *et al.* Interface engineering for high-performance, triple-halide perovskite–silicon tandem solar cells. *Science* **381**, 63–69 (2023).

[6] Al-Ashouri, A. *et al.* Monolithic perovskite/silicon tandem solar cell with¿ 29% efficiency by enhanced hole extraction. *Science* **370**, 1300–1309 (2020).

[7] Jiang, Q. *et al.* Surface passivation of perovskite film for efficient solar cells. *Nature Photonics* **13**, 460–466 (2019).

[8] Zhang, S. *et al.* Minimizing buried interfacial defects for efficient inverted perovskite solar cells. *Science* **380**, 404–409 (2023).

[9] Dou, L. *et al.* Atomically thin two-dimensional organic-inorganic hybrid perovskites. *Science* **349**, 1518–1521 (2015).

[10] Lee, J.-W., Tan, S., Seok, S. I., Yang, Y. & Park, N.-G. Rethinking the a cation in halide perovskites. *Science* **375**, eabj1186 (2022).

[11] Zhao, Y. *et al.* Suppressing ion migration in metal halide perovskite via interstitial doping with a trace amount of multivalent cations. *Nature Materials* **21**, 1396–1402 (2022).

[12] Li, C. *et al.* Rational design of lewis base molecules for stable and efficient inverted perovskite solar cells. *Science* **379**, 690–694 (2023).

[13] Wang, R. *et al.* Constructive molecular configurations for surface-defect passivation of perovskite photovoltaics. *Science* **366**, 1509–1513 (2019).

[14] Song, K. *et al.* Atomic-resolution imaging of halide perovskites using electron microscopy. *Advanced Energy Materials* **10**, 1904006 (2020).

[15] Yang, S. *et al.* Stabilizing halide perovskite surfaces for solar cell operation with wide-bandgap lead oxysalts. *Science* **365**, 473–478 (2019).

[16] Ball, J. M. & Petrozza, A. Defects in perovskite-halides and their effects in solar cells. *Nature Energy* **1**, 1–13 (2016).

[17] Zhang, D. *et al.* Atomic-resolution transmission electron microscopy of electron beam–sensitive crystalline materials. *Science* **359**, 675–679 (2018).

[18] Rothmann, M. U. *et al.* Atomic-scale microstructure of metal halide perovskite. *Science* **370**, eabb5940 (2020).

[19] Zhang, S. *et al.* Deterministic synthesis of a two-dimensional mapbi3 nanosheet and twisted structure with moiré superlattice. *Journal of the American Chemical*

*Society* **146**, 27861–27870 (2024).

[20] Pennycook, T. J. *et al.* Efficient phase contrast imaging in stem using a pixelated detector. part 1: Experimental demonstration at atomic resolution. *Ultramicroscopy* **151**, 160–167 (2015).

[21] Pennycook, T. J., Martinez, G. T., Nellist, P. D. & Meyer, J. C. High dose efficiency atomic resolution imaging via electron ptychography. *Ultramicroscopy* **196**, 131–135 (2019).

[22] Zhang, H. *et al.* Three-dimensional inhomogeneity of zeolite structure and composition revealed by electron ptychography. *Science* **380**, 633–638 (2023).

[23] Chen, Z. *et al.* Mixed-state electron ptychography enables sub-angstrom resolution imaging with picometer precision at low dose. *Nature communications* **11**, 2994 (2020).

[24] Sha, H. *et al.* Ptychographic measurements of varying size and shape along zeolite channels. *Science Advances* **9**, eadf1151 (2023).

[25] Song, J. *et al.* Atomic resolution defocused electron ptychography at low dose with a fast, direct electron detector. *Scientific reports* **9**, 3919 (2019).

[26] Jannis, D. *et al.* Event driven 4d stem acquisition with a timepix3 detector: Microsecond dwell time and faster scans for high precision and low dose applications. *Ultramicroscopy* **233**, 113423 (2022).

[27] Jannis, D., Velazco, A., Béché, A. & Verbeeck, J. Reducing electron beam damage through alternative STEM scanning strategies, Part II: Attempt towards an empirical model describing the damage process. *Ultramicroscopy* **240**, 113568 (2022).

[28] Maiden, A. M. & Rodenburg, J. M. An improved ptychographical phase retrieval algorithm for diffractive imaging. *Ultramicroscopy* **109**, 1256–1262 (2009).

[29] Maiden, A. M., Mei, W. & Li, P. WASP: Weighted average of sequential projections for ptychographic phase retrieval. *Optics Express* **32**, 21327–21344 (2024).

[30] Gao, C. *et al.* Overcoming contrast reversals in focused probe ptychography of thick materials: An optimal pipeline for efficiently determining local atomic structure in materials science. *Applied Physics Letters* **121** (2022).

[31] Clark, L. *et al.* The effect of dynamical scattering on single-plane phase retrieval in electron ptychography. *Microscopy and Microanalysis* **29**, 384–394 (2023).

[32] Hofer, C., Gao, C., Chennit, T., Yuan, B. & Pennycook, T. J. Phase offset method of ptychographic contrast reversal correction. *Ultramicroscopy* **258**, 113922 (2024).

[33] Zhang, S. *et al.* Moiré superlattices in twisted two-dimensional halide perovskites. *Nature Materials* **23**, 1222–1229 (2024).

[34] Quarti, C., De Angelis, F. & Beljonne, D. Influence of surface termination on the energy level alignment at the ch3nh3pbi3 perovskite/c60 interface. *Chemistry of Materials* **29**, 958–968 (2017).

[35] Mirzehmet, A. *et al.* Surface termination of solution-processed ch3nh3pbi3 perovskite film examined using electron spectroscopies. *Advanced Materials* **33**,

2004981 (2021).

[36] Kim, T. *et al.* Mapping the pathways of photo-induced ion migration in organic-inorganic hybrid halide perovskites. *Nature Communications* **14**, 1846 (2023).